

Supporting Information

**Supporting Information includes: Experimental Section, Figure S1-S15, Table S1-S3
and Reference 1-40**

High-Performance Metal Halide Perovskite-Based Laser-Driven Display†

Shaoan Zhang^{a,b,c,#}, Zhenzhang Li^{a,b,c,#}, Zaijin Fang^d, Bao Qiu^f, Janak L. Pathak^b, Kaniyarakkal Sharafudeen^g, S. Saravanakumar^h, Zhanjun Li^b, Gang Han^{*e}, Yang Li^{*b,c}

^a*Faculty of Electrical Engineering and Computer Science, Ningbo University, Ningbo 314211, China.*

^b*School of Biomedical Engineering, Guangzhou Medical University, Guangzhou 511436, China.*

^c*School of Optoelectronic Engineering, Guangdong Polytechnic Normal University, Guangzhou 510665, China.*

^d*Guangdong Provincial Key Laboratory of Optical Fiber Sensing and Communications, Institute of Photonics Technology, Jinan University, Guangzhou 511443, China.*

Department of Biochemistry and Molecular Pharmacology, University of Massachusetts Medical School, Worcester, Massachusetts 01605, USA.

^f*Ningbo Institute of Materials Technology & Engineering (NIMTE), Chinese Academy of Sciences, Ningbo 315201, China.*

^g*Kuwait College Science and Technology, Doha 27335, Kuwait.*

^h*Department of Physics, Kalasalingam University, Krishnan Koil, Viridhunagar, 626126, Tamil Nadu, India.*

Corresponding Authors

*Ganghan@umassmed.edu

*lychris@sina.com

1. Experimental Section

1.1 Materials

Cesium bromide (CsBr, 99.5%), lead bromide (PbBr₂), N, N-dimethylformamide (DMF, 99.5%), cyclohexane, and ethyl acetate (EA, 99%) were obtained from Sigma-Aldrich. In this experiment, straight-chain primary amine was selected as ligands such as octylamine (C₈, 99%), decylamine (C₁₀, 99%), dodecylamine (C₁₂, 99%), tetradecylamine (C₁₄, 99%), hexadecylamine (C₁₆, 99%) and oleylamine (C₁₈, 99%), which are also purchased from the Sigma-Aldrich. All these chemicals were used without any further purification.

1.2 Synthesis of Cs₄PbBr₆@CsPbBr₃ MHPs

Before the experiment, it is necessary to check the air tightness of the synthetic system. First, CsBr (1.2768 g, 6 mmol) and PbBr₂ (0.3670 g, 1 mmol) were loaded into a 50 ml three-necked flask and then degassed for about one hour with high purity nitrogen (N₂). During the experiment, 10 mL DMF was transferred into the three-necked flask as the temperature rise, and then 2 ml oleylamine was also injected. The reaction temperature was kept at 90 °C and maintained for 10 min under the N₂ atmosphere. Finally, Cs₄PbBr₆@CsPbBr₃ MHPs were washed three times with EA and cyclohexane, collected by centrifugation at 5000 rpm for 10 min and then dried at around 60°C for 24 h in a vacuum oven. Similarly, by substituting oleylamine with 1 mL octylamine, decylamine, dodecylamine, tetradecylamine, and hexadecylamine for oleylamine, other Cs₄PbBr₆@CsPbBr₃ MHPs were synthesized by the above experiment process.

1.3 Characterization Techniques

For insight into the detailed composition of Cs₄PbBr₆@CsPbBr₃ MHPs, powder X-ray diffraction (XRD) patterns were carried out in a range of 10-90° with the X-ray diffractometer (Bruker D₈ Advance, Cu Kα1 radiation), where the scanning step is set to be 0.02° and the scanning rate is fixed to be 5°/min. Temperature-dependent *in situ* XRD patterns were also collected by the known Bruker D₈ Advance X-ray

diffractometer. Photoluminescence excitation (PLE), and emission (PL) spectra were carried out on an Edinburgh Instruments' FLS 1000 spectrophotometer with a red-sensitive photomultiplier (Hamamatsu R928P) in a Peltier cooled housing of which a 450 W ozone-free xenon. Decay curves were also collected by the FLS 1000 spectrophotometer with a nF900 flash lamp as the excitation source. By coating MHP-C₈ onto the sapphire glass, PL spectra of our prepared MHP-C₈ sample dependent on the power density of blue LD were measured with a home-made optical test platform. The illuminance of the LD driven white-light device was measured in a cold room (15-18 °C). The internal quantum efficiencies of all samples were measured using the integrated sphere on the same FLS 1000 instrument using the high purity BaSO₄ powder as a reference. The morphology and microstructure of Cs₄PbBr₆@CsPbBr₃ MHPs were recorded using a field-emission scanning electron microscope (Hitachi SU8220, Japan) and transmission electron microscope (JEOL JEM 2100F). The high-temperature PL spectra ranging from RT to 573 K were collected by Ocean spectrophotometer connected with a home-made heating equipment. The internal quantum efficiencies of all samples were measured using the integrated sphere on the same FLS 1000 instrument using the high purity BaSO₄ powder as a reference. The morphology and microstructure of Cs₄PbBr₆@CsPbBr₃ MHPs were recorded using a field-emission scanning electron microscope (Hitachi SU8220, Japan) and transmission electron microscope (JEOL JEM 2100F). Temperature-dependent *in situ* Fourier transform infrared (FTIR) spectra were recorded on a UV-3600plus Spectrometer (Thermo IS 50). X-ray photoelectron spectroscopy (XPS) spectra were measured using an electron spectrometer (VG ESCALABMK II) with a Mg K α (1200 eV) line as an excitation source. Thermal gravimetric analysis (Instrument model: Mettler Toledo TGA) was performed under a N₂ atmosphere with a heating rate of 10 °C/min.

To obtain the relative adsorption content of ligands on MHP solids, the detail for the sample preparation method and test process is described as follows: first, a series of MHP solids were weighed to the same quality (2.0 mg), and mixed thoroughly with the pure KBr solid powder (400.0 mg) in sequence, respectively. The mixed powders

are pressed into plates of equal size and thickness by the same mold. During the tests, argon gas was used to protect these plates from oxygen and water in the air.

1.4 Computational Methods

1.4.1 DFT calculations

In this work, theoretical calculation results were obtained by combining the density functional theory (DFT) with the projector augmented wave (PAW) method, which was carried out with the Vienna *ab initio* simulation package (VASP).^[1-2] In this approach, the exchange-correlation energy was approximated using the generalized gradient approximations (GGA) of Perdew-Burke-Ernzerhof (PBE). The energy cutoff is set to be 550 eV for the PAW basis functions. A 10×8×2 Monkhorst-pack mesh is performed for integrations over the Brillouin zone.^[3] All the tests, cutoff, k mesh, and supercell size ensure the convergence for defect formation energies to be within ±0.2 eV.^[4] For each supercell, all internal parameters are allowed to relax until the forces acting on each atom are converged to within 0.01 eV/Å.

1.4.2 Illuminance calculation of an area light source:

$$E = \frac{d\phi}{dA} = \frac{L \cdot dA_s \cos \theta_1 \cos \theta_2}{r^2}$$

where L is the brightness of the light source; θ_1 and θ_2 are the angle between the normal line of the luminous surface dA_s and the illuminated surface dA and the distance r direction, respectively.^[5] Supposing that L is fixed at 3500 cd/m², the length and width of the outdoor large screen is set as 4 m and 2 m, and the screen is 0.5 m above the ground, respectively.

1.5 LD Fabrications

Firstly, the mixture of Cs₄PbBr₆@CsPbBr₃ MHPs, commercial red phosphor (K₂SiF₆:Mn⁴⁺) and transparent epoxy resin was coated onto a high thermal conductivity sapphire glass which is located away from the heat source of the laser diode. Then, LD device is assembled with a blue laser diode, radiator shell and sapphire glass. The photoelectric parameters such as color rendering index (CRI), color temperature (CT) and Commission International de l'Eclairage 1931 chromaticity (CIE) of high-power LD

device were performed on a photoelectric test system (HASS 2000) with an integrating sphere spectroradiometer system.

2. Supplementary Figures (S1-S15)

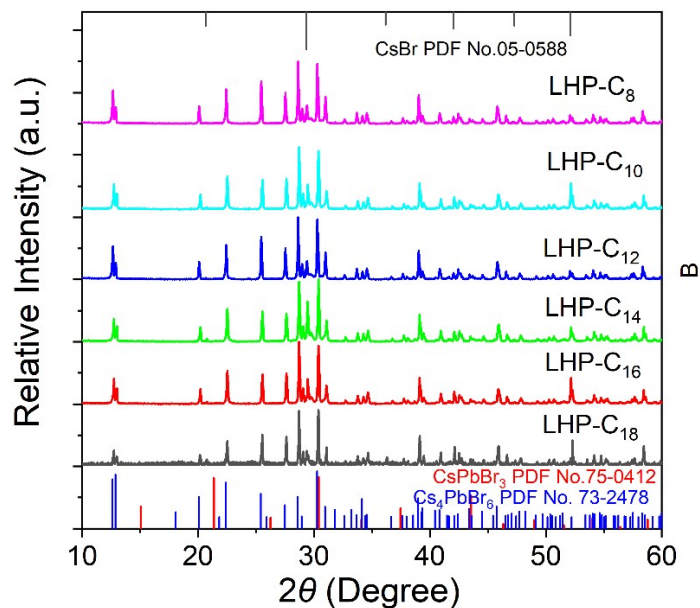


Figure S1. XRD patterns of MHP-C₈, MHP-C₁₀, MHP-C₁₂, MHP-C₁₄, MHP-C₁₆ and MHP-C₁₈ solids.

Figure S1 shows XRD patterns of MHP-C₈, MHP-C₁₀, MHP-C₁₂, MHP-C₁₄, MHP-C₁₆ and MHP-C₁₈ solids. From **Figure S1**, the diffraction intensity at 31°, which is ascribed to CsPbBr₃, is much lower than that of Cs₄PbBr₆, indicating that CsPbBr₃ nanocrystals are embedded into the Cs₄PbBr₆ host. Meanwhile the diffraction peak at 29.4° originates from the residual CsBr, which can not affect the PL performance of MHP solids.

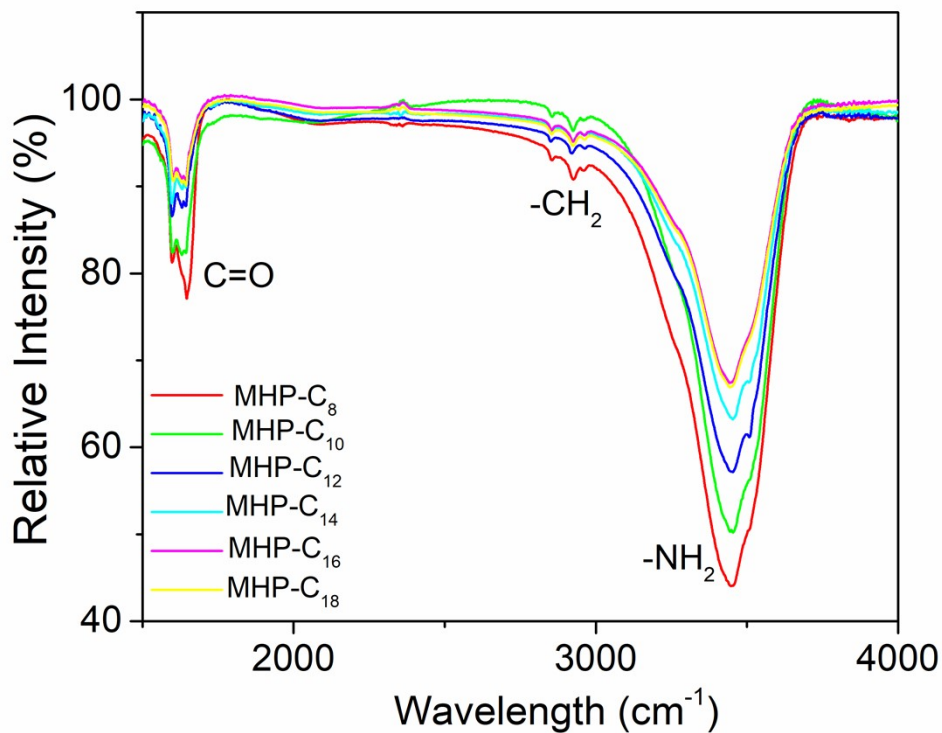


Figure S2. FTIR spectra of MHP-C₈, MHP-C₁₀, MHP-C₁₂, MHP-C₁₄, MHP-C₁₆ and MHP-C₁₈ solids.

The absorption peaks at 3486 cm⁻¹ originates from the interaction between R-NH₂ and V_{Br-} of Cs₄PbBr₆@CsPbBr₃ solids, which can reflect the relative adsorption content of the absorbed ligands. As shown in **Figure S2**, it is inferred that the relative content of the adsorption primary amines on the surface of Cs₄PbBr₆@CsPbBr₃ solids decreased with the lengthening of the carbon chain. These results confirm the relative content of C₈ adsorbed on the surface of Cs₄PbBr₆@CsPbBr₃ solids is the largest.

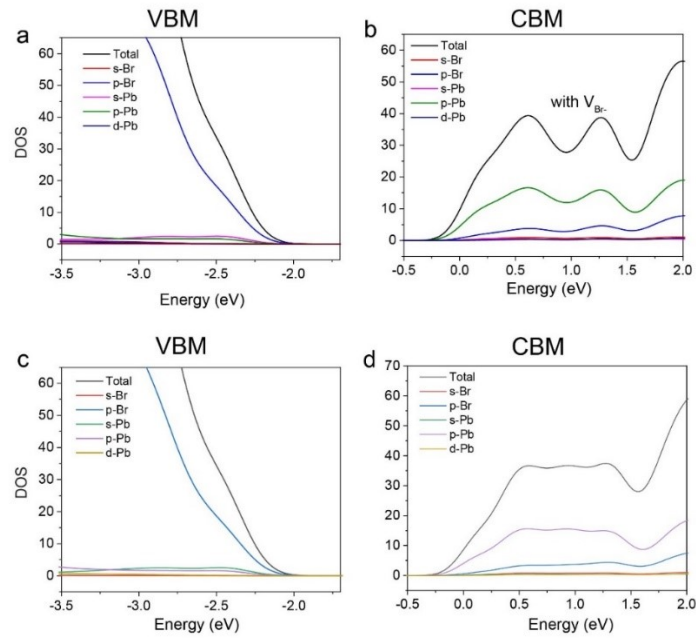


Figure S3. Density of states (DOS) of valence band maximum (VBM) and conduction band minimum (CBM) of CsPbBr₃ with V_{Br-} (a, b) and octylamine-modified CsPbBr₃ (c, d).

(R3) To further demonstrate the key role of octylamine on the elimination of V_{Br-} defects, it was observed that electronic structure (VBM) of CsPbBr₃ with V_{Br-} (**Figure S3a**) was identical with that of octylamine-modified CsPbBr₃ (**Figure S3c**), indicating no influence of V_{Br-} defects on VBM. However, DOS curves of Pb 6p and 6d ranging from 0.5 to 1.5 eV was rough not smooth (**Figure S3b**), indicating the existence of V_{Br-} defect level. Meanwhile, the final DOS curves after the coordination of octylamine almost in **Figure S3d** are smooth which is similar to that of CsPbBr₃ perfect crystal. By comparing DOS curves between CsPbBr₃ with V_{Br-} (**Figure S3b**) and octylamine-modified CsPbBr₃ (**Figure S3d**), it is concluded that octylamine as the ligands serves as the “Br-Pb” binding-like status and effectively recovers the V_{Br-}-induced trapping states [8]. Therefore, octylamine as the capping ligand suppress the generation of defects.

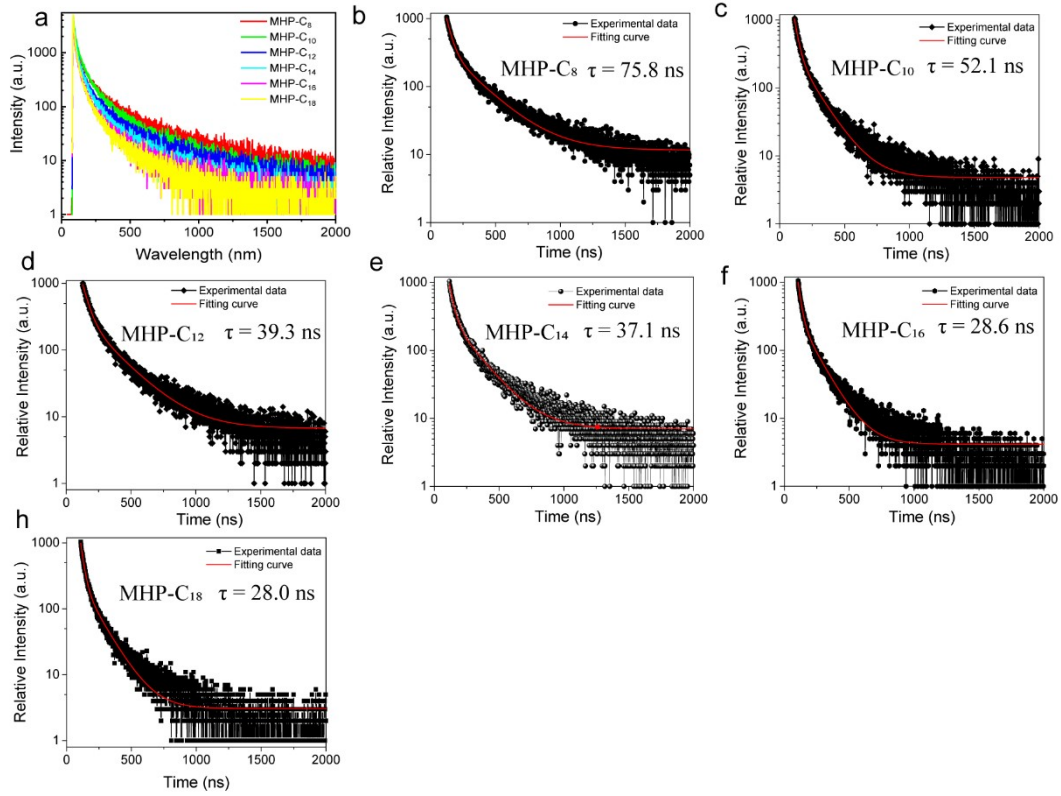


Figure S4. Decay and fitting curves of MHP-C₈, MHP-C₁₀, MHP-C₁₂, MHP-C₁₄, MHP-C₁₆ and MHP-C₁₈ solids.

Figure S4a exhibits the decay curves of MHP-C₈, MHP-C₁₀, MHP-C₁₂, MHP-C₁₄, MHP-C₁₆ and MHP-C₁₈ solids. From **Figure S4a**, it can be concluded that the decay lifetimes of MHP-C₈, MHP-C₁₀, MHP-C₁₂, MHP-C₁₄, MHP-C₁₆ and MHP-C₁₈ solids shorten with the lengthening of the carbon chain. **Figure S4b-h** give the fitting line and luminescence lifetimes of MHP-C₈, MHP-C₁₀, MHP-C₁₂, MHP-C₁₄, MHP-C₁₆ and MHP-C₁₈ solids. The τ_{ave} values of MHP were shortened from 75.8 to 28.0 ns as the carbon chain lengthens from C₈ to C₁₈, indicating that the shorter the carbon chain of the ligands, the less the number of surface defects. It is worth noting that the decay curves of MHP are all subject to the biexponential decay, and the average lifetime (τ) of MHP is calculated by the following equation [9, 10]:

$$\tau_{\text{ave}} = \frac{\int_0^{\infty} I(t) t dt}{\int_0^{\infty} I(t) dt} \quad (1)$$

The τ_{ave} value of MHP-C₈, MHP-C₁₀, MHP-C₁₂, MHP-C₁₄, MHP-C₁₆ and MHP-C₁₈ solids is 75.8, 52.1, 39.3, 37.1, 28.6 and 28.0 ns.

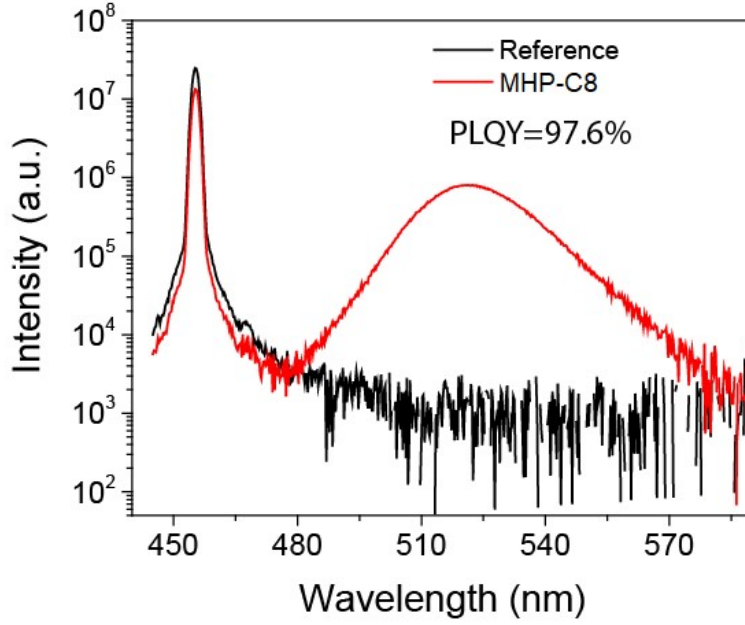


Figure S5. PLQY of our prepared MHP-C₈ solids under excitation with 450 nm blue light.

As we know, η_{IQE} is defined as the ratio of the number of emitted photons to that of absorbed photons. Thus, η_{IQE} value of the MHP-C₈ solids was estimated by the following equation (1) [11, 12]:

$$\eta_{IQE} = \frac{\int L_s}{\int E_R - \int E_S} \quad (2)$$

where $\int L_s$, $\int E_R$ and $\int E_S$ represent the fluorescence integral intensities of emission, background and excitation spectrum, respectively. Based on the above equations (2), η_{IQE} value of the MHP-C₈ solids was calculated to be 97.6% (**Figure S5**).

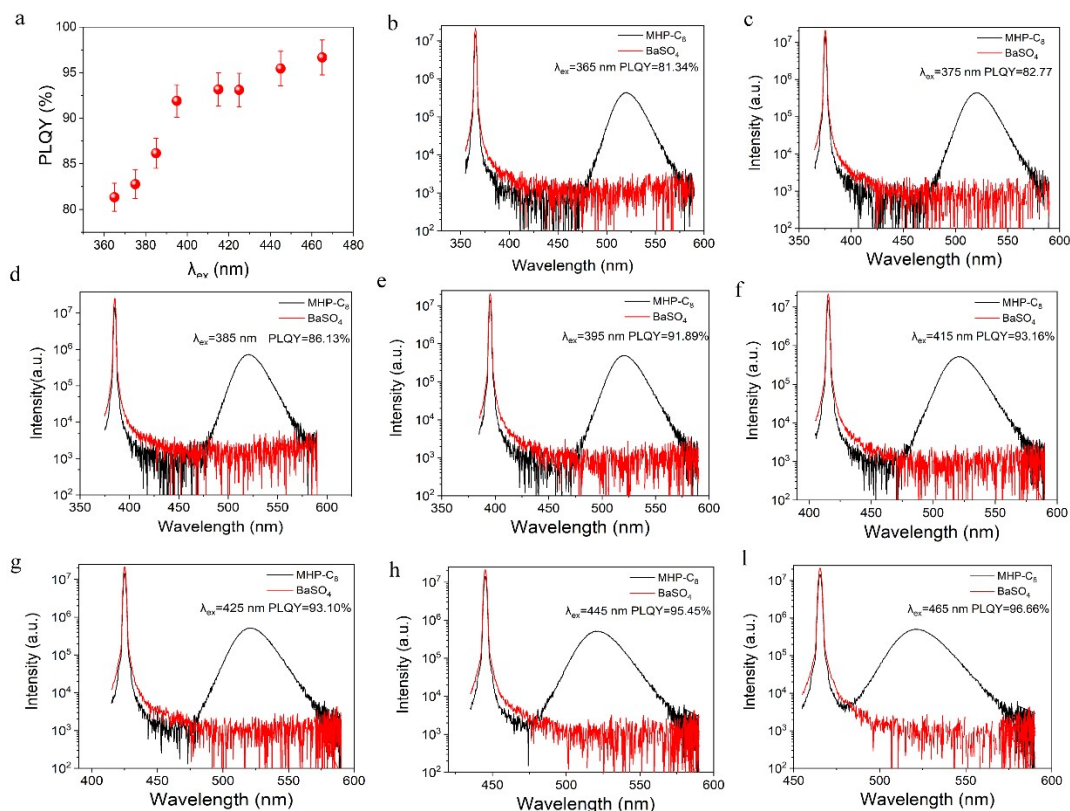


Figure S6. Dependence of PLQY of MHP-C₈ solids on the excitation wavelength.

In **Figure S6**, one can see that PLQY of MHP-C₈ solids increases with the lengthening of the excitation wavelength. The PLQY (81.34%) was obtained under excitation with 365 nm, and it gradually increases with the increase of the excited wavelength (λ_{exc}). It is notable that the highest PLQY reaches as high as 96.66% under excitation at 465 nm.

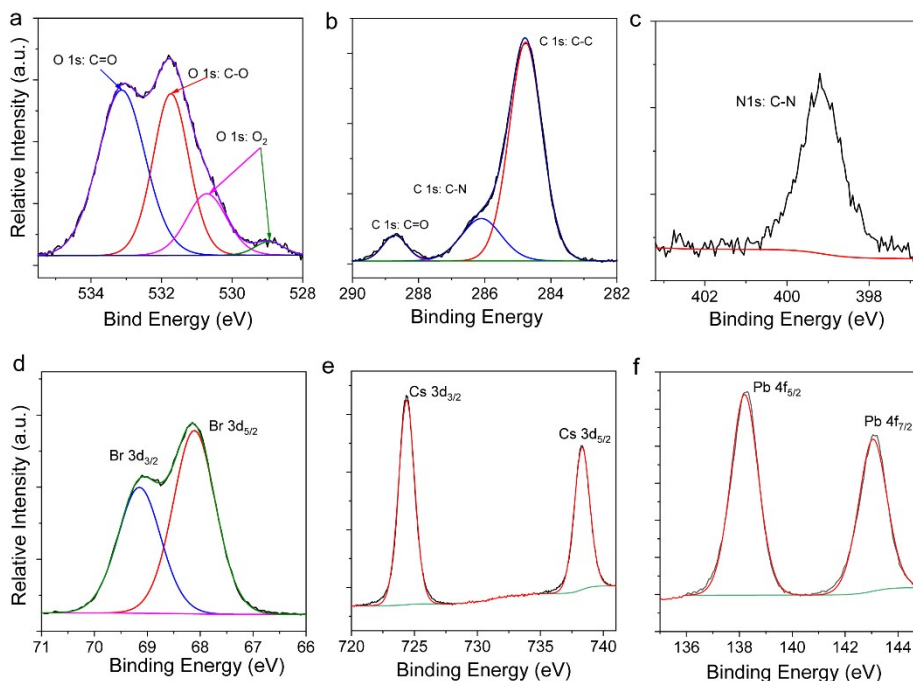


Figure S7 (a-f). XPS refined curves of O 1s, C 1s, C-N, Br 3d, Cs 3d and Pb 4f, respectively.

Figure S7 show the XPS refined curves of O 1s, C 1s, C-N, Br 3d, Cs 3d and Pb 4f, respectively. To deeply analyze the surface compositions of $\text{Cs}_4\text{PbBr}_6:\text{CsPbBr}_3\text{-C}_8$, **Figure S7** present the high-resolution chemical states of C 1s, N 1s, O 1s, Br 3d, Cs 3d, and Pb 4f, respectively. In **Figure S7a**, the fitted peaks of O 1s chemical state at 533.14 and 531.76 eV are ascribed to C=O and C-O chemical states. Chemical states at 530.72 and 528.94 eV are attributed to the 1s state of O_2 . In **Figure S7b**, there are three fitted peaks of C 1s at 288.67, 286.07 and 284.74 eV, which are attributed to the C=O, C-N and C-C chemical states, respectively. C=O chemical state originates from the carbonyl group of DMF, while C-C chemical states mainly derive from the short chains of octylamine. In **Figure S7c**, only one peak of N 1s chemical state at 399.02 eV directly confirms the presence of octylamine on the surface of MHP- C_8 . In **Figure S7d-f**, Br 3d, Cs 3d, and Pb 4f chemical states are observed, which originate from the $\text{Cs}_4\text{PbBr}_6:\text{CsPbBr}_3$ solids. Thus, it is confirmed that both DMF and octylamine exist on the surface of $\text{Cs}_4\text{PbBr}_6:\text{CsPbBr}_3$.

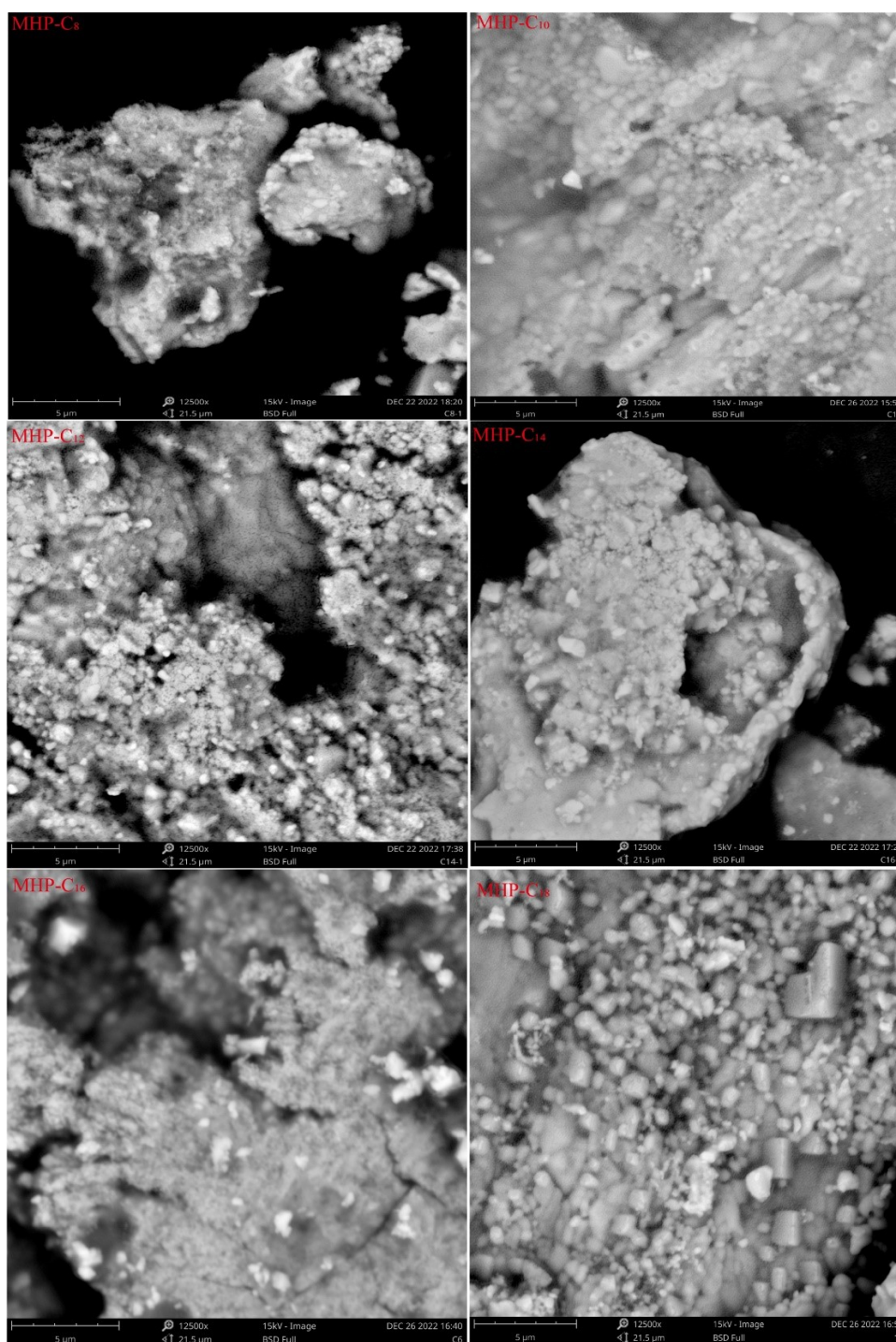


Figure S8. SEM images of MHP-C₈, MHP-C₁₀, MHP-C₁₂, MHP-C₁₄, MHP-C₁₆ and MHP-C₁₈.

To show the morphology and particle size of MHP-C₈, MHP-C₁₀, MHP-C₁₂, MHP-C₁₄, MHP-C₁₆ and MHP-C₁₈ solids, SEM was carried out to characterize the morphology of MHP solids. SEM images in **Figure S8** show that all MHP solids are made up of tiny particles condensed together.

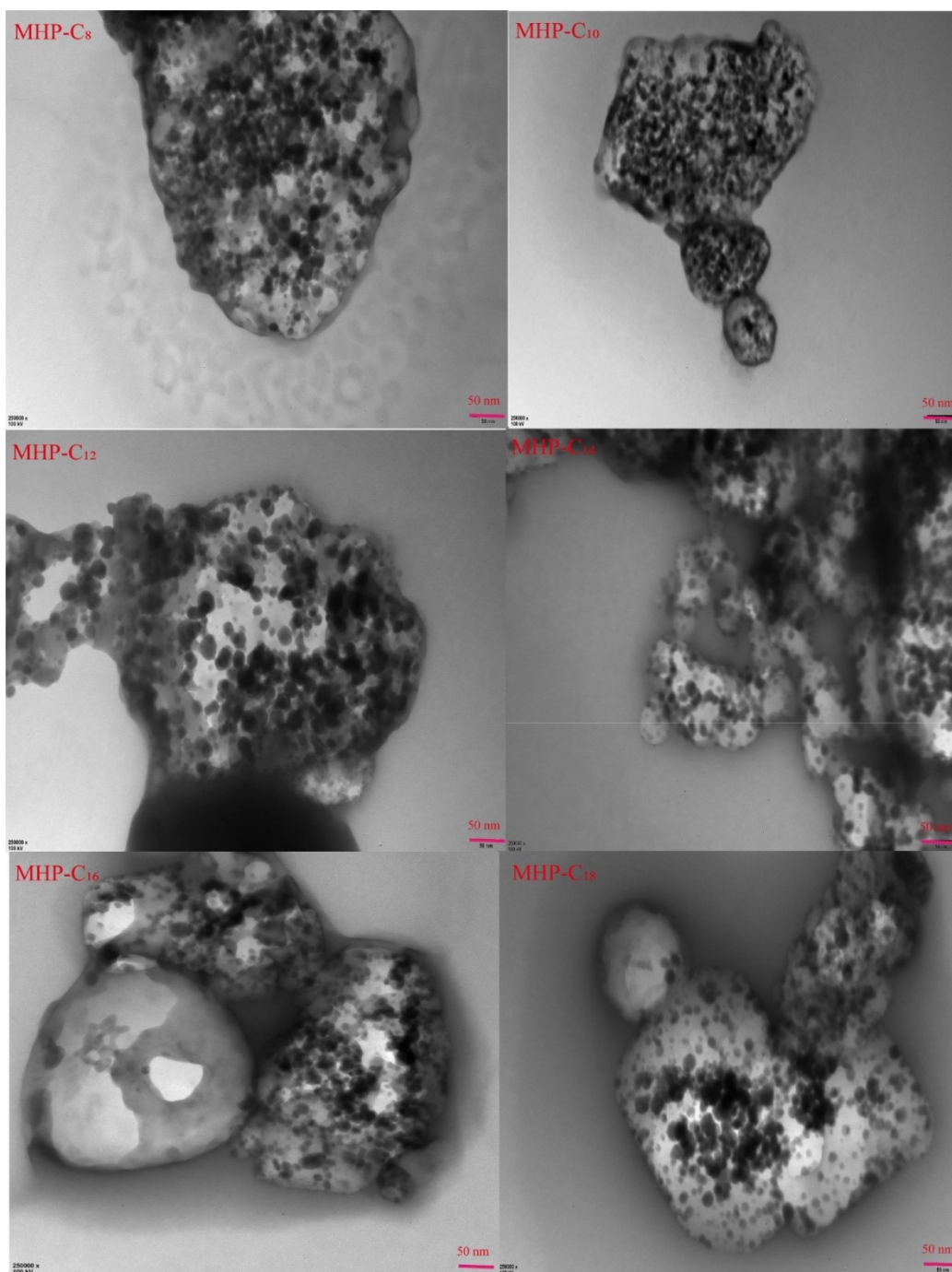


Figure S9. TEM images of MHP-C₈, MHP-C₁₀, MHP-C₁₂, MHP-C₁₄, MHP-C₁₆ and MHP-C₁₈.

In order to study the morphology more clearly, all MHP solids were ultrasonically shaken for 30 minutes, and then the supernatant suspension was extracted and observed by TEM. TEM images (**Figure S9**) show that agglomerated large particles are constituted by a large number of small spherical particles, while the spherical particles are bonded together by organic layers. Based on the SEM and TEM results, it is observed the morphology and particle size of all MHP solids are similar.

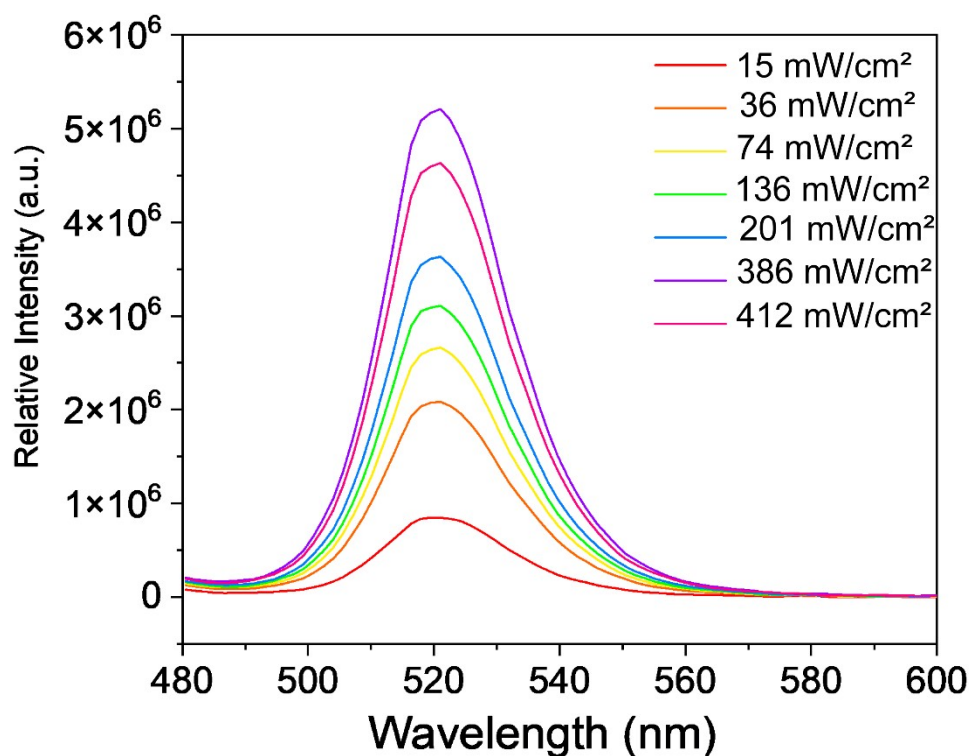


Figure S10. PL spectra of our prepared MHP-C₈ sample dependent the on power density of blue LD.

As shown in **Figure 10**, PL intensity of MHP-C₈ solids steadily increases with the increasing power density of blue LD. However, once over the threshold (386 mW/mm²) of blue LD, PL intensity of MHP-C₈ solids starts to decrease due to the thermal quenching. It is notable that MHP-C₈ solids were coated onto the sapphire glass, and then these PL spectra were collected with the FLS 1000 spectrophotometer.

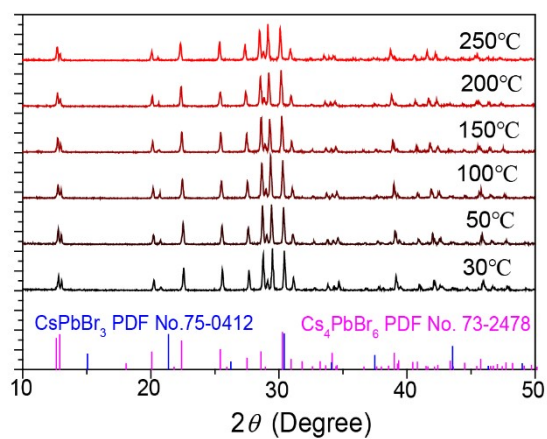


Figure S11. Temperature-dependent in situ XRD patterns of MHP-C8 ranging from 30-250 °C

In **Figure S11**, no new Bragg reflections of in situ XRD patterns are observed and the intensity of all Bragg reflections does not change from RT to 250 °C, indicating the high thermal tolerance of MHP-C₈ solids.

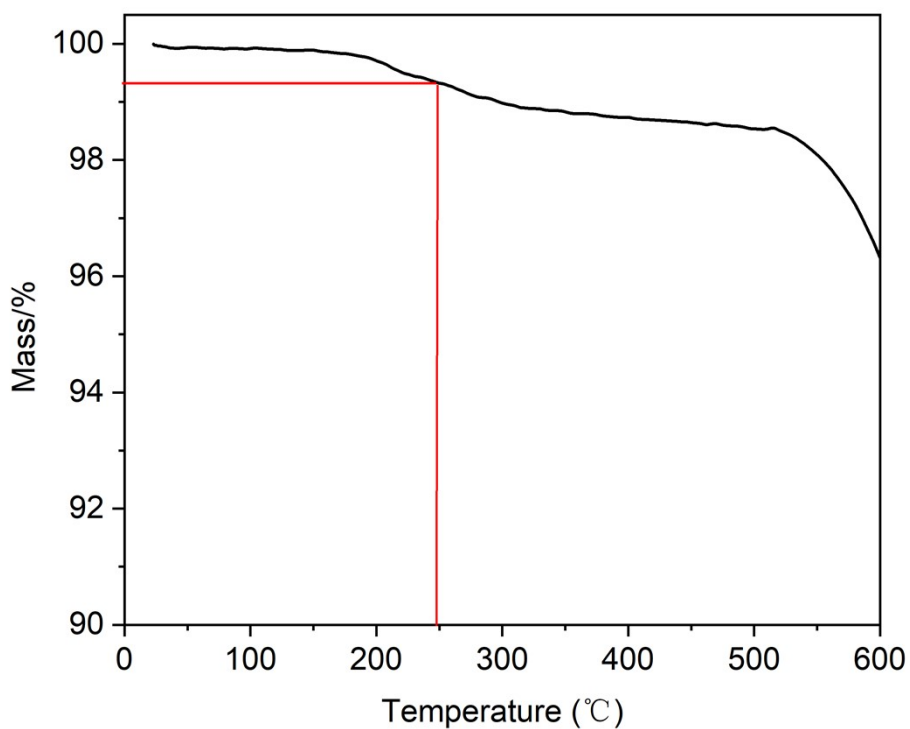


Figure S12. Thermogravimetric analysis of MHP-C₈ solid.

TG curves were performed under a N₂ atmosphere in a Perkin-Elmer instrument; the heating rate is 10 °C/min. One can see that a small weight loss in the temperature range of 0-250 °C is less than 1% in **Figure S12**, which is attributed to the evaporation of water and light organic components (DMF).

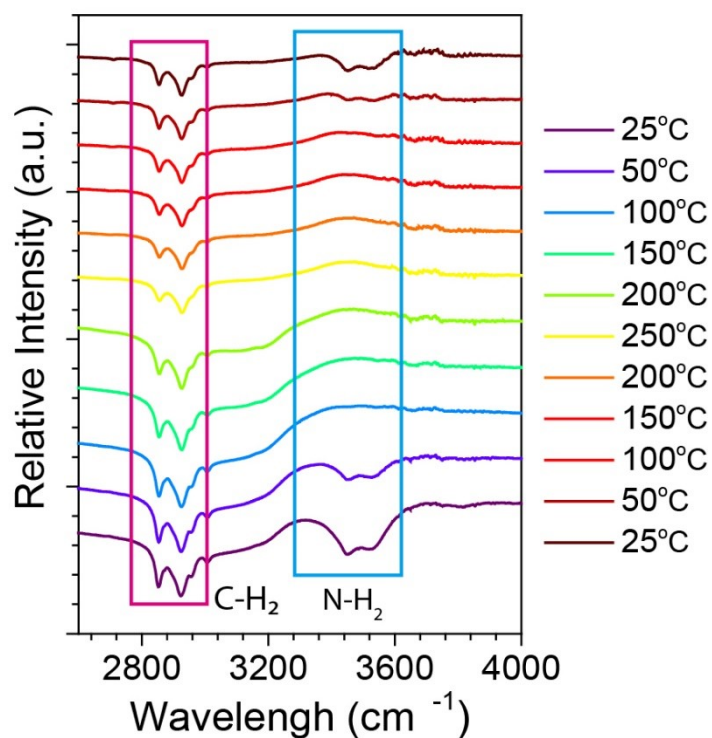


Figure S13. *In situ* FTIR spectra of MHP-C₁₈ dependent on the changing temperature.

In **Figure S13**, there is an absorption intensity of MHP-C₁₈ solid at 2915 cm⁻¹, which is attributed to the hydrocarbon chains with methyl $-(\text{CH}_2)_n-$, and little effect of the increasing temperature is observed on this absorption at 2915 cm⁻¹. The absorption intensity at 3486 cm⁻¹ gradually attenuates until they disappear in the heating process from 25 °C to 250 °C, implying the fracture of surface coordination bonds between R-NH₂ and V_{Br}. In the cooling process, the absorption intensity at 3486 cm⁻¹ gradually recovers, however, only partial recovery when cooling to room temperature.

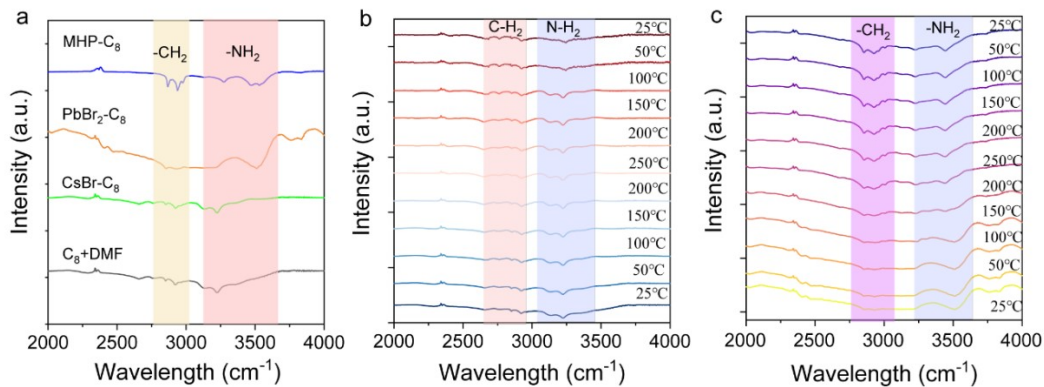


Figure S14. (a) FTIR spectra of C₈+DMF solution, CsBr-C₈, PbBr₂-C₈ and MHP-C₈ solids; (b, c) Temperature-dependent *in situ* FTIR spectra of CsBr-C₈ and PbBr₂-C₈, respectively.

Indeed, high thermal tolerance and photostability of MHP-C₈ solids originate from the structural self-healing ability. Such structural self-healing ability is attributed to the fracture and intact of surface coordination bonds between R-NH₂ and V_{Br}. To prove this conjecture, a comparison of the temperature-dependent *in situ* FTIR spectra among MHP-C₈, CsBr-C₈, and PbBr₂-C₈ was conducted. **Figure S14a** shows the characteristic stretching vibration peaks of MHP-C₈, CsBr-C₈, and PbBr₂-C₈ at room temperature. It is worth noting that the stretching vibration peaks of functional group N-H₂ in CsBr-C₈ sample are consistent with that in C₈ solution, indicating that there is no interaction between CsBr and C₈. However, the stretching vibration of -N-H in PbBr₂-C₈ and MHP-C₈ are different from that in C₈ solution, implying the occurrence of interaction between PbBr₂ and C₈.

In **Figure S14b**, the absorption peaks at 2764 and 2853 cm⁻¹ originate from C-H₂ stretching vibration of the carbon chain, indicating the absorption of C₈ on the surface of MHP solids. The absorption peaks at 3129 and 3225 cm⁻¹ are ascribed to the N-H wagging of C₈. The vibrational mode of N-H at 3129 and 3225 cm⁻¹ did not change in the heating-cooling process (25°C → 250°C → 25°C), indicating that no interaction between CsBr and C₈ occurs in this heating-cooling process. In temperature-dependent *in situ* FTIR spectra of PbBr-C₈, the absorption peak at 3446 cm⁻¹ in **Figure S14c** becomes weak gradually in heating (25°C → 250°C), and become increasing gradually in the cooling process (250°C → 25°C). these absorption peaks at 3228 and

3446 cm^{-1} infers the interaction between PbBr_2 and C_8 . The interaction between PbBr_2 and C_8 derives from bridging bond between the lone pair electron of nitrogen and the empty orbital in the outermost shell of lead. ^[13,14] By combining with the disappearance and reappearance of $-\text{NH}_2$ absorption peak in MHP-C_8 , these results demonstrate that such structural self-healing ability is attributed to the fracture and intact of surface coordination bonds between R-NH_2 and $\text{V}_{\text{Br}\cdot}$. ^[13,14]

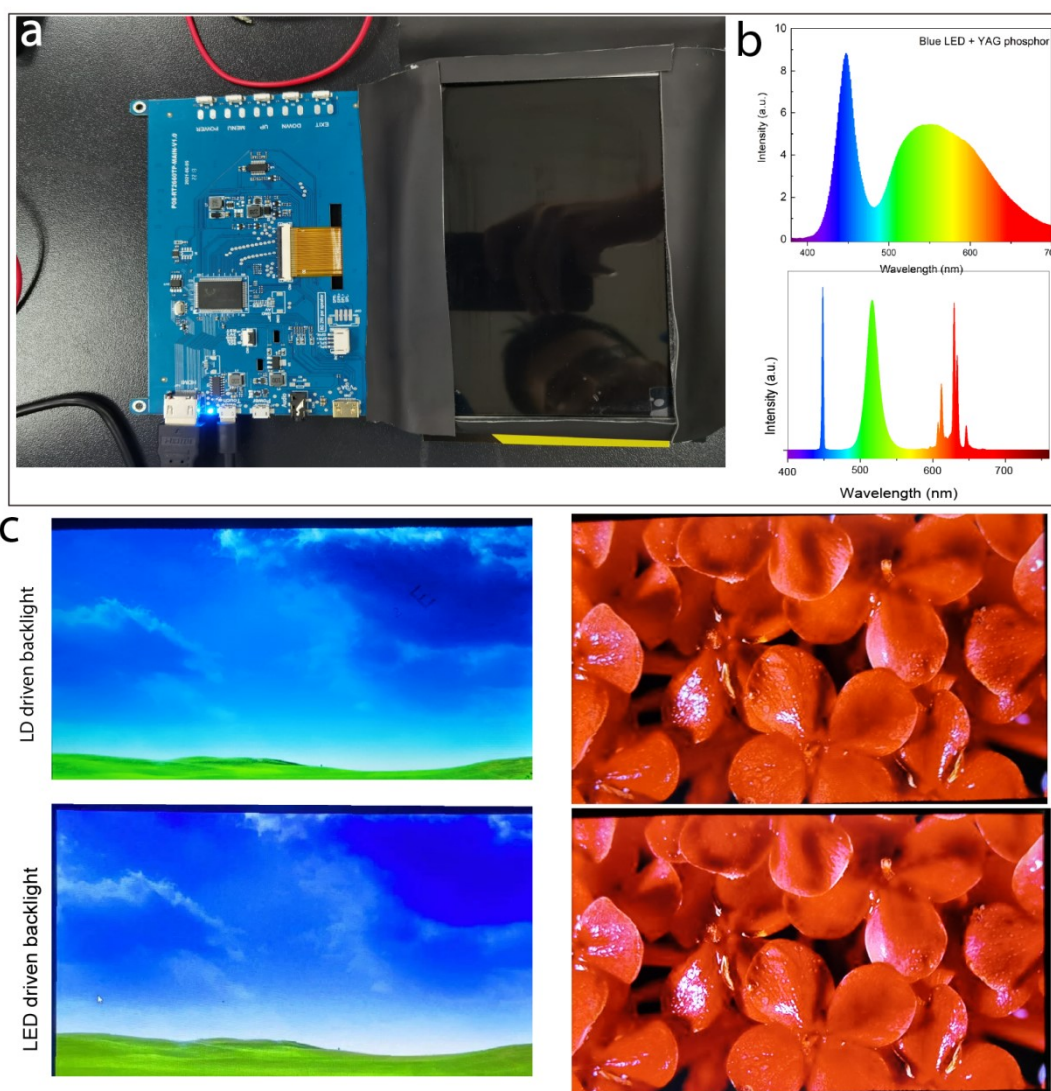


Figure S15. (a) LD-driven LCD display model; (b) EL spectra of commercial white backlight and LD driven white backlight; (c) blue and red pictures displayed by commercial white backlight and LD driven white backlight.

Figure S15a shows the LD driven LCD display prototype consisting of the commercial circuit board and display screen. **Figure S15b** shows the EL spectra of commercial white backlight and LD driven white backlight. It is notable that LD emission in the blue region exhibits a narrower full width at half maximum than that of the blue LED. **Figure S15c** exhibits blue and red pictures displayed by commercial white backlight and LD driven white backlight, respectively.

3. Supplementary Tables S1-S3

Table S1. PLQY and stability of CsPbBr₃ solids prepared by different methods (PLQY corresponding to the excitation wavelength at a blue light (450 nm)).

Composition	PLQY	PL Stability	Synthetic method	Ref.
CsPbBr ₃ @β-zeolite	61%	treating under a 150 °C treatment, soaking in water over 30 days, as well as applying in 450 nm light-emitting devices (LED) for 20 days	high temperature solid-state method	[15]
CsPbBr ₃ @NH ₄ Br	64%	40% (3.5h, water)	Hot-injection, ion-exchange	[16]
CsPbBr ₃ @Al ₂ O ₃	70%	80% after 12 h heating at 300 °C	high temperature solid-state confined growth strategy	[17]
CsPbBr ₃ @SiO ₂	71%	PL intensity keeps 100% with 450 nm LED light irradiation for 1000 h	High temperature; SiO ₂ encapsulation	[18]
CsPbBr ₃ @CsPb ₂ Br ₅	80%	45% (110 h, water)	Endotaxial systems	[19]
CsPbBr ₃ @PMMA	82.7%	PL was unchanged after 90 h of UV irradiation or 35 days of heating at 60 °C	<i>in situ</i> polymeric melt encapsulation method	[20]
MAPbBr ₃ /SiO ₂	89%	61% (49, illuminated with 450 nm LED light)	Hot-injection, TMOS hydrolysis	[21]
CsPbBr ₃ @Cs ₄ PbBr ₆	90%		a solution-phase synthesis	[22]
CsPbBr ₃ @Pb ₃ (PO ₄) ₂	95%	PL intensity unchanged at ambient condition (20 °C and 60% humidity) after one week	one-pot reprecipitation method	[23]
CsPbBr ₃ @Cs ₄ PbBr ₆ -C ₈	97.6%	PL intensity after multiple heating-cooling cycles (30 times) from RT to high temperature (250 °C), under long-term blue light irradiation (12 h) with a high-power density (386 mW/mm ²)	a straightforward heterogeneous interfacial method	this work

Table S2. CIE color coordinates for NTSC 1953 standard, commercial backlit display and CsPbBr₃@Cs₄PbBr₆ backlit display.

	Blue Coordinate (x, y)		Green Coordinate (x, y)		Red Coordinate (x, y)		Area
NTSC 1931	0.14	0.08	0.21	0.71	0.67	0.33	0.1582
NTSC 2020	0.131	0.046	0.17	0.797	0.708	0.292	0.2118
Commercial Display	0.1495	0.0423	0.3142	0.6007	0.6227	0.3396	0.1076
White LDs	0.1492	0.0247	0.1334	0.7822	0.6917	0.3082	0.2077

Table S3. A comparison of phosphor-converted white LEDs and our designed white LD as LCD backlights.

Components of the backlight			Color gamut	Refs
Blue	Green	Red		
Blue LED	RbLi(Li ₃ SiO ₄) ₂ :Eu ²⁺	KSF:Mn ⁴⁺	107% (NTSC 1931)	[24]
Blue LED	CsPbBr ₃ /Cs ₄ PbBr ₆ /PMMA film	CdSe/CdS/PMMA film	111.4% (NTSC 1931)	[25]
Blue LED	CsPbBr ₃ /Cs ₄ PbBr ₆ crystals	KSF:Mn ⁴⁺	90.6% (Rec. 2020)	[26]
Blue LED	MAPbBr ₃ @SiO ₂ /PVDF	KSF:Mn ⁴⁺	121% (NTSC 1931)	[27]
Blue LED	MAPbBr ₃ /PVDF	KSF:Mn ⁴⁺	121% (NTSC 1931)	[28]
Blue LD	CsPbBr ₃ /CsPb ₂ Br ₅	KSF:Mn ⁴⁺	95.8% (Rec. 2020)	[29]
m-Blue LED	CsPbBr ₃ QDs	CdSe QDs	129% (NTSC1931)	[30]
Blue LED	CsPbBr ₃ @glass	CsPbBr _{1.5} 1.5@glass	127% (NTSC 1931)	[31]
Blue LED	CsPbBr ₃ QD@glass	K ₂ SiF ₆ :Mn ⁴⁺	124% (NTSC 1931)	[32]
Blue LED	CsPbBr ₃ /m-SiO ₂	K ₂ SiF ₆ :Mn ⁴⁺	92% (NTSC 1931)	[33]
Blue LED	CsPbBr ₃ nanocrystals	K ₂ SiF ₆ :Mn ⁴⁺	128% (NTSC 1931)	[34]
Blue LED	CsPbBr ₃ /Cs ₄ PbBr ₆	K ₂ SiF ₆ :Mn ⁴⁺	119% (NTSC 1931)	[35]
Blue LED	CsPbBr ₃ @glass film	KSF:Mn ⁴⁺	130% (NTSC 1931)	[36]
Blue LED	CsPbBr ₃ @SiO ₂	CsPbBr _{1.2} 1.8@PMMA	112% (NTSC1931)	[37]
Blue LED	CsPb ₂ Br ₅ /CsPbBr ₃ @glass	CsPbBr _{1.2} 1.8@PMMA	130% (NTSC 1931)	[38]
Blue LED	CsPbBr ₃ @Kaolin	CaAlSiN ₃ :Eu ²⁺	111% (NTSC1931)	[39]
Blue LED	CsPbBr ₃ @SiO ₂	CsPbBr _{1.2} 1.5@SiO ₂	111% (NTSC1953)	[40]
Blue LD	MHP-C ₈ powders	KSF:Mn ⁴⁺	132% (NTSC1931) 98% (Rec. 2020)	This work

4. Supplementary References 1-40

- [1].G. Kresse, J. Furthmüller, Phys. Rev. B 1996, 54, 11169-11186;
- [2].J.P. Perdew, K. Burke, M. Ernzerhof, Phys. Rev. Lett. 1996, 77, 3865-3868;
- [3].P.E. Blochl, Phys. Rev. B **1994**, 50, 17953-17979;
- [4].T. Matsuzawa, Y. Aoki, N. Takeuchi, Y. Murayama, J. Electrochem. Soc. 1996,143, 2670-2673.
- [5].R. H. Simons, A.R. Bean, Simons, Lighting Engineering: Applied Calculations (1st ed.). Routledge.
- [6].Q. Zhong, M. Cao, Y. Xu, P. Li, Y. Zhang, H. Hu, D. Yang, Y. Xu, L. Wang, Y. Li, X. Zhang, Q. Zhang, Nano Lett. 2019, 19, 4151.
- [7].C. Giansante, I. Infante, J. Phys. Chem. Lett. 2017, 8, 5209.
- [8].D. Yang, X. Li, W. Zhou, S. Zhang, C. Meng, Y. Wu, Y. Wang, H. Zeng, Adv. Mater. 2019, 31, e1900767.
- [9].J. Xu, P. Li, D. R. Onken, C. Dun, Y. Guo, K. B. Ucer, C. Lu, H. Wang, S.M. Geyer, R. T. Williams, and D. L. Carroll, Adv. Mater. 2017, 29, 1703703.
- [10].R. T. Liu, X. P. Zhai, Z. Y. Zhu, B. Sun, D. W. Liu, B. Ma, Z. Q. Zhang, C. L. Sun, B. L. Zhu, X. D. Zhang, Q. Wang, H. L. Zhang, J. Phys. Chem. Lett. 2019, 10, 6572.
- [11].H. Lian, Y. Li, K. Sharafudeen, W. Zhao, G. R. Krishnan, S. Zhang, J. Qiu, K. Huang, G. Han, Adv. Mater. 2020, e2002495.
- [12].S. Zhang, B. Qiu, Z. Li, Y. Lv, X. Chen, H. Lian, Y. Hu, Y. Li, Chem. Eng. J. 2021, 426.
- [13].Wen, J. R. Roman, B. J. Rodriguez Ortiz, F. A. Mireles Villegas, N. Porcellino, N. Sheldon, M. Chem. Mater. 2019, 31, 8551.
- [14].Quarta, D. Imran, M. Capodilupo, A.L. Petralanda, U. Beek van, B. De Angelis, F. Manna, L. Infante, I. De Trizio, L. Giansante, C. J. Phys. Chem. Lett. 2019, 10, 3715.
- [15].B. Li, Y. Zhang, Y. Xu, Z. Xia, J. Mater. Chem. C 2021, 9, 12118.
- [16].S. Lou, T. Xuan, C. Yu, M. Cao, C. Xia, J. Wang, H. Li, J. Mater. Chem. C 2017, 5, 7431.
- [17].B. Wang, C. Zhang, W. Zheng, Q. Zhang, Z. Bao, L. Kong, L. Li, Chem. Mater. 2020, 32, 308.
- [18].Z. Wang, R. Fu, F. Li, H. Xie, P. He, Q. Sha, Z. Tang, N. Wang, H. Zhong, Adv. Funct. Mater. 2021, 31, 2010009.
- [19].S. Lou, Z. Zhou, T. Xuan, H. Li, J. Jiao, H. Zhang, R. Gautier, J. Wang, ACS Appl. Mater. Interfaces 2019, 11, 24241.
- [20].K. Ma, X.-Y. Du, Y.-W. Zhang, S. Chen, J. Mater. Chem. C 2017, 5, 9398.
- [21].S. Huang, Z. Li, L. Kong, N. Zhu, A. Shan, L. Li, J. Am. Chem. Soc. 2016, 138, 5749.
- [22].L. N. Quan, R. Quintero-Bermudez, O. Voznyy, G. Walters, A. Jain, J. Z. Fan, X. Zheng, Z. Yang, E. H. Sargent, Adv. Mater. 2017, 29.
- [23].J. Liu, Q. Zhong, S. Chen, W. Guan, Y. Qiu, D. Yang, M. Cao, Q. Zhang, J. Mater. Chem. C 2021, 9, 466.
- [24].M. Zhao, H. Liao, L. Ning, Q. Zhang, Q. Liu, Z. Xia, Adv. Mater. 2018, 30, e1802489.
- [25].M. Su, B. Fan, H. Li, K. Wang, Z. Luo, Nanoscale 2019, 11, 1335.
- [26].X. Chen, F. Zhang, Y. Ge, L. Shi, S. Huang, J. Tang, Z. Lv, L. Zhang, B. Zou, H. Zhong, Adv. Funct. Mater. 2018, 28, 1706567.
- [27].Y. Huang, F. Li, L. Qiu, F. Lin, Z. Lai, S. Wang, L. Lin, Y. Zhu, Y. Wang, Y. Jiang, X.

- Chen, ACS Appl. Mater. Interfaces 2019, 11, 26384-26391.
- [28].Q. Zhou, Z. Bai, W.-g. Lu, Y. Wang, B. Zou, H. Zhong, Adv. Mater. 2016, 28, 9163-9168.
- [29].S. Lou, Z. Zhou, W. Gan, T. Xuan, Z. Bao, S. Si, Y. Y. Cao, H. L. Li, Z.Go. Xia, J.B.Qiu, J. Wang, Green Chem. 2022, 22, 5257-5261.
- [30].Y. Yin, Z. Hu, M. U. Ali, M. Duan, L. Gao, M. Liu, W. Peng, J. Geng, S. Pan, Y. Wu, J. Hou, J. Fan, D. Li, X. Zhang, H. Meng, Adv. Mater. Technol. 2020, 5, 2000251.
- [31].J. Lin, Y. Lu, X. Li, F. Huang, C. Yang, M. Liu, N. Jiang, D. Chen, ACS Energy Lett. 2021, 6, 519.
- [32].J. Li, Y. Fan, T. Xuan, H. Zhang, W. Li, C. Hu, J. Zhuang, R. S. Liu, B. Lei, Y. Liu, X. Zhang, ACS Appl. Mater. Interfaces 2022, 14, 30029.
- [33].Z. Liu, L. Sinatra, M. Lutfullin, Y. P. Ivanov, G. Divitini, L. De Trizio, L. Manna, Adv. Energy Mater. 2022, 12, 2201948.
- [34].Y. Zhang, G. Li, G. Hou, J. Lin, M. Chen, S. Liu, H. Lin, J. Fang, C. Jing, J. Chu, Chem. Eng. J. 2022, 438, 135270.
- [35].V. Naresh, T. Jang, Y. Pang, N. Lee, Nanoscale 2022, 14, 17789.
- [36].J. Lee, H. Lee, U. Kim, W. J. Chung, W. B. Im, J. Mater. Chem. C, 2023,11, 898-902.
- [37]. X.T. Liu, W. Chen, J. Yang, X. Liang, X. Fang, W. Xiang, ACS Appl. Electron. Mater. 2023, 5, 4, 2309-2317.
- [38]. Y. Chen, E. Mei, X. Liang, Q. Chen, W.D. Xiang, J. Lumin. 2023, 253, 119456.
- [39].X. L. Zeng, L. Yu, K. Peng, Y. Yu, Y. Deng, Y. Zhao, Y. Xu, J. Alloys. Comd. 2023, 945, 169213.
- [40].S. Chen, J. Lin, S. Zheng, Y. Zheng, D. Chen, Adv. Funct. Mater. 2023, 33, 2213442